Astronomy & Astrophysics

Detection of a new sample of Galactic white dwarfs in the direction of the Small Magellanic Cloud

A. V. Sidharth[1,★] , B. Shridharan[1,3] , B. Mathew[1,★], A. Devaraj[1] , T. B. Cysil[1] , C. S. Stalin[2] ,
R. Arun[2] , S. Bhattacharyya[1] , S. S. Kartha[1], and T. Robin[1]

[1] Department of Physics and Electronics, CHRIST (Deemed to be University), Bangalore 560029, India
[2] Indian Institute of Astrophysics, Sarjapur Road, Koramangala, Bangalore 560034, India
[3] Tata Institute of Fundamental Research, Homi Bhabha Road, Mumbai 400005, India

ABSTRACT

Aims. In this study, we demonstrate the efficacy of the Ultraviolet Imaging Telescope (UVIT) in identifying and characterizing white dwarfs (WDs) within the Milky Way Galaxy.
Methods. Leveraging the UVIT point-source catalogue towards the Small Magellanic Cloud and cross-matching it with *Gaia* DR3 data, we identified 43 single WDs (37 new detections), 13 new WD+main-sequence candidates, and 161 UV bright main-sequence stars by analysing their spectral energy distributions. Using the WD evolutionary models, we determined the masses, effective temperatures, and cooling ages of these identified WDs.
Results. The masses of these WDs range from 0.2 to 1.3 $M_\odot$ and the effective temperatures (T_{eff}) lie between 10 000 K to 15 000 K, with cooling ages spanning 0.1–2 Gyr. Notably, we detect WDs that are hotter than reported in the literature, which we attribute to the sensitivity of UVIT. Furthermore, we report the detection of 20 new extremely low-mass candidates from our analysis. Future spectroscopic studies of the extremely low-mass candidates will help us understand the formation scenarios of these exotic objects. Despite limitations in *Gaia* DR3 distance measurements for optically faint WDs, we provide a crude estimate of the WD space density within 1kpc of 1.3×10^{-3} pc^{-3}, which is higher than previous estimates in the literature.
Conclusions. Our results underscore the instrumental capabilities of UVIT and anticipate forthcoming UV missions such as INSIST for systematic WD discovery. Our method sets a precedent for future analyses in other UVIT fields to find more WDs and perform spectroscopic studies to verify their candidacy.

Key words. techniques: photometric – binaries: general – Hertzsprung–Russell and C–M diagrams – white dwarfs – ultraviolet: stars

1. Introduction

White dwarfs (WDs) are the end stages of stellar evolution for the majority of main-sequence (MS) stars with masses lower than 8 M$_\odot$, which end their life by dissipating their remnant energy and cool down (Fontaine et al. 2001). The census and characterisation of WDs have witnessed significant advancements, propelled by the use of various optical surveys such as *Gaia* Data Release 2 (DR2) (Gaia Collaboration 2018), *Gaia* Data Release 3 (DR3) (Brown et al. 2021), and the Sloan Digital Sky Survey (SDSS) (York et al. 2000). Gentile Fusillo et al. (2019, 2021), Kepler et al. (2016, 2019, 2021), and Eisenstein et al. (2006) have significantly refined our understanding of WDs. Accurate parallax measurements from *Gaia* DR2 and DR3 have revolutionised the study of WDs, enabling an unprecedented scale of the search for these stellar remnants. Jiménez-Esteban et al. (2018) identified ~73 000 WD candidates by delving into a detailed exploration of the population within the 100 pc solar neighbourhood. Extending this effort, Gentile Fusillo et al. (2019) used *Gaia* DR2 to identify ~260 000 WD candidates, and Gentile Fusillo et al. (2021) presented a compilation of ~359 000 high-confidence WD candidates spanning the entire sky using *Gaia* EDR3.

On the other hand, hot WDs (with $T_{eff} \geq$ 10 000 K) remained elusive in these optical surveys because they have a low optical luminosity and the optical colours are insensitive to hotter temperatures (Gómez de Castro & Barstow 2007). The operation of the Galaxy Evolution Explorer (GALEX) ultraviolet sky survey (Morrissey et al. 2007), Bianchi et al. (2011) used GALEX to identify hot WDs in the Milky Way. UV point-source catalogues are invaluable gateways into the studies of UV-bright MS stars, blue straggler stars (BSS), yellow straggler stars, sub–subgiants, WDs, and white dwarf – MS (WD+MS) binary systems (Bianchi 2009; Bianchi et al. 2011; Parsons et al. 2016; Rebassa-Mansergas et al. 2017; Subramaniam et al. 2018; Ren et al. 2020). The UV surveys, in combination with optical photometry, help us to characterize these systems and understand the end stages of stellar evolution. Rebassa-Mansergas et al. (2021) studied WD+MS systems using *Gaia* EDR3 to identify a volume-limited sample of 112 unresolved WD+MS binaries within 100 pc. Combining astrometric and photometric data from *Gaia* DR3 with GALEX GR6/7, Nayak et al. (2024) identified 93 WD+MS candidates. Recently, Jackim et al. (2024) presented the GALEX – *Gaia* EDR3 catalogue, which contains 332 111 candidate WD binary systems and 111 996 candidate single WDs.

The Ultra Violet Imaging Telescope (UVIT) on board the AstroSat mission is a suite of far-UV (FUV; 130–180 nm),

★ Corresponding authors; sidharthnarayanan17@gmail.com;
blesson.mathew@christuniversity.in

near-UV (NUV; 200–300 nm), and visible band (VIS; 320–550 nm) imagers. UVIT can perform simultaneous observations in these three channels with a field of view (FoV) diameter of ~28′ and an angular resolution of 1.5–1.8″ (more details on UVIT can be found in Kumar et al. 2012; Tandon et al. 2017a, and Tandon et al. 2017b). The higher angular resolution of UVIT compared to the 4.2–5.3″ angular resolution of GALEX (Morrissey et al. 2007) and the availability of seven filters in the UV range (1161–2882 Å) compared to two filters in GALEX help us characterise WD systems with a higher precision than previous studies conducted using GALEX. Previous studies using UVIT observations have identified WDs and WD binary systems in open clusters and globular clusters, as evident from a series of UVIT open cluster studies (e.g. Panthi & Vaidya 2024; Panthi et al. 2023; Vaidya et al. 2022; Sindhu et al. 2019; Jadhav et al. 2019) and Globular Cluster UVIT Legacy Survey (GlobULeS) studies (e.g. Dattatrey et al. 2023a,b; Prabhu et al. 2022; Sahu et al. 2022), thus showcasing the superior capabilities of the UVIT instrument.

In this study, we use the UVIT point-source catalogue from Devaraj et al. (2023) to explore the FUV (1300–1800 Å) and NUV (2000–3000 Å) observations directed towards a previously less explored line of sight towards the Small Magellanic Cloud (SMC). As a follow-up to the UVIT point-source catalogue provided by Devaraj et al. (2023), we cross-match them with the *Gaia* DR3 catalogue (Gaia Collaboration 2023). This allows us to combine the photometric data from seven UV filters and the optical photometry and astrometry from *Gaia* DR3 in order to identify and characterise the UV bright sources in the FoV of the SMC. The availability of seven UV data points allows the generation of a better fit to the spectral energy distributions (SED), providing more accurate parameters.

The manuscript is structured as follows. In Sect. 2, we describe the data we used in this study and discuss the method we employed to cross-match the UVIT point-source catalogue with *Gaia* DR3. Section 3 presents the method for identifying MS, WD, and WD+MS systems in our sample. Furthermore, by combining UV photometry with available optical photometry, we fit the SED of each source to characterise the identified sources. We estimate the mass and cooling ages of our WD and WD+MS candidates and compare these parameters with values from the literature. Section 4 discusses the identification of extremely low-mass WD (ELM) candidates in our sample. We also discuss the completeness of our WD identification and its implications on WD space density estimates. A summary of our findings is given in Sect. 5.

2. Data

We made use of the UVIT point-source catalogue (hereafter, SMC-UVIT-1), which includes the observations taken at three fields with a combined FoV of ~40′ towards the SMC (centred at $\alpha_{2000} = $ ~17.285° and $\delta_{2000} = $ ~−71.329°), between 2017 December 31 and 2018 January 1 (Devaraj et al. 2023). The three fields were shifted ~6′ in an orthogonal direction from each other, with some level of overlap between them. The first field was chosen far away from the centre of the SMC to avoid the bright central region (Tandon et al. 2020). Figure 1 shows the greyscale mosaic of the three SMC fields observed by UVIT in the N245M filter. UVIT has an impressive ~1.5″ spatial resolution that is better than the ~5″ spatial resolution of GALEX or the ~3″ spatial resolution of the Ultraviolet Imaging Telescope (UIT) (Stecher et al. 1997). For further details on the exposure
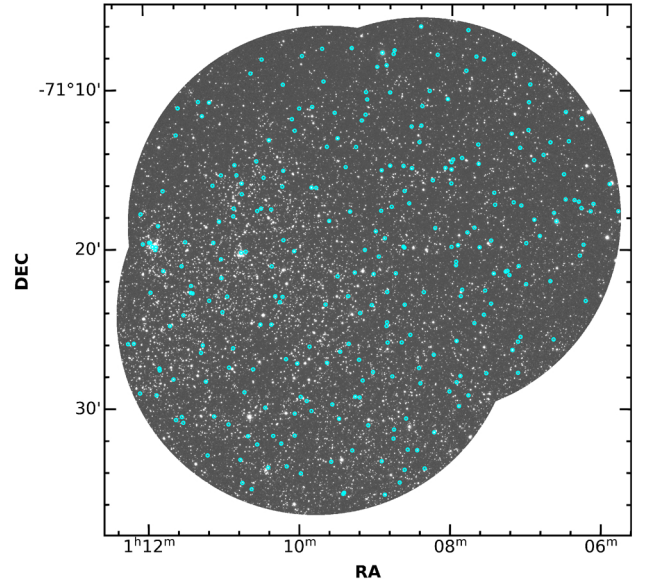
Fig. 1. Greyscale mosaic of the three SMC fields observed by UVIT in the N245M filter. The image was convolved by a Gaussian kernel of 1.5″ for better visualisation. The sample of 273 sources in this study is shown as open cyan circles.

time and the information on different filters we used, refer to Devaraj et al. (2023). SMC-UVIT-1 has a combined total of 11 241 objects detected across seven UVIT filters, that is, F154W, F169M, F172M, N245M, N263M, N279N, and N219M, with a limiting magnitude of ~21 mag.

We cross-matched the SMC-UVIT-1 and *Gaia* DR3 catalogue[1] to complement our UV data with astrometric and optical photometric information. The cross-matching was performed by employing a search radius of 1.5″ that was aligned with the spatial resolution of the UVIT instrument. This resulted in a source list of 10 847 objects for which both UVIT and *Gaia* measurements are available (hereafter SMC-UVIT-*Gaia*). The average offset in angular separation between the corresponding UVIT and *Gaia* sources is about 0.1″, and ~90% of the sources match within 0.4″.

We applied the following astrometric and photometric quality criteria to the *Gaia* DR3 catalogue, adapted from Rebassa-Mansergas et al. (2021):

- $I_{BP}/\sigma_{I_{BP}} \geq 10$
- $I_{RP}/\sigma_{I_{RP}} \geq 10$
- $I_G/\sigma_{I_G} \geq 10$
- $\varpi/\sigma_\varpi \geq 3$
- $\varpi > 0$,

where ϖ is the parallax in arcseconds, I_G, I_{BP}, and I_{RP} are the fluxes in the bandpass filters G, G_{BP}, and G_{RP}, respectively, and the σ values are the standard errors of the corresponding parameters. Furthermore, we applied the following photometric quality criterion to the available UVIT magnitudes:

- $M_X/\sigma_{M_X} \geq 10$,

where M_X and σ_{M_X} represent the magnitude and the error in magnitude in each of the seven UVIT filters. Not all stars have UVIT magnitudes in all seven filters.

From the sample of 10 847 sources, 273 sources met the given criteria, and 87.9% of the sources have a renormalised unit weight error (RUWE) ≤ 1.4. About 76% of 273 sources have data
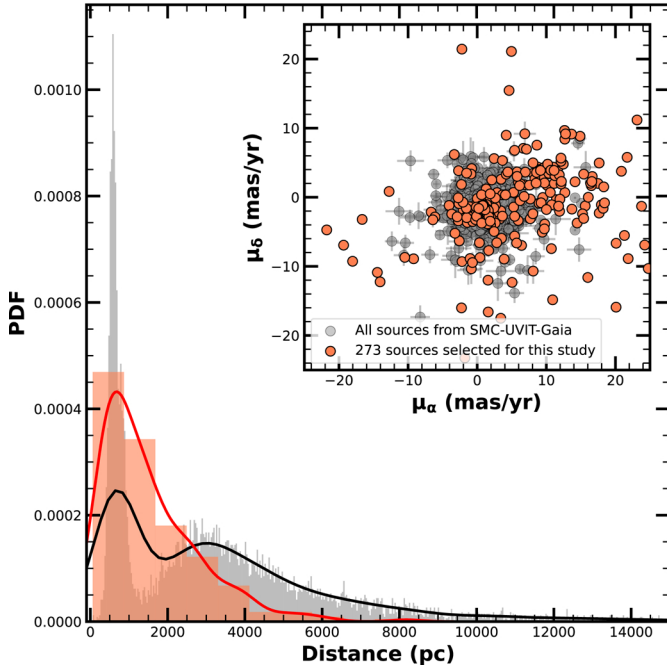
[1] https://gea.esac.esa.int/archive/

Fig. 2. *Gaia* DR3 distance (Bailer-Jones et al. 2021) distribution plot of the 273 sources used in this study. The 273 sources used in this study are shown in orange, and the 10 847 sources in the SMC-UVIT-*Gaia* are shown as grey markers. The kernel density estimates of the distributions are overlaid for better visual representation. The red and black lines show the kernel density estimates of the 273 sources and SMC-UVIT-*Gaia* sources, respectively. In the inset we show a scatter plot with error bars of the proper motion in RA (mas/yr) vs. proper motion in Dec (mas/yr). For most sources, the error bars have the size of the markers.

in at least three UV filters in addition to the three *Gaia* optical filters. This dataset, which is comprised of 273 sources with robust photometric and astrometric information, was used in this study. A list of these 273 sources, along with their UVIT magnitudes, is given in Table A.1.

3. Analysis and results

3.1. Do the sources belong to the Small Magellanic Cloud or to the Milky Way?

A critical aspect of our analysis is to discern whether our sample of 273 sources belong to the SMC or if they are Milky Way (MW) sources projected on the line of sight to the SMC. To accomplish this, we leveraged the distance data provided by *Gaia* DR3 for all the sources (Bailer-Jones et al. 2021), which are depicted as a histogram in Fig. 2. Our 273 sources lie within the distance range of 50–6500 pc, and the maximum distance is recorded at 8176 ± 769 pc. Notably, the SMC is situated at a distance of 61.9 ± 0.6 kpc (De Grijs & Bono 2015), establishing a stark contrast between the distances of our sources and the known distance of the SMC. In addition to the distance values, from the plot of the proper motion in Dec (μ_δ) versus proper motion in RA (μ_α) given in Fig. 2 (inset), it is clear that the majority of 273 sources have higher values than the rest of the SMC-UVIT-*Gaia* sources. This confirms that the 273 sources belong to the MW, and they are found to be in the projection of the SMC.

Furthermore, to have an understanding of the types of sources in our sample, we performed a SIMBAD cross-match of the 273 sources and found that 24 sources have previous classifications in the literature. We note that 6 sources are classified as WD candidates (WD*_candidate) by Gentile Fusillo et al. (2021). Out of these six WD candidates, *Gaia* DR2 4690619477160130944 was also listed as a WD candidate in Jiménez-Esteban et al. (2018). Thirteen sources are classified as 'stars'. Two sources are classified as '*RGB*_candidate', one as RR Lyrae Variable (RRLyr), one as a high proper motion star (*PM**), and one as a Classical Cepheid Variable (deltaCep). We also cross-matched our list of 273 sources with the WD catalogue provided by Jackim et al. (2024) and found 12 matches. One of the sources classified as a WD candidate by Jackim et al. (2024) was also classified as a WD candidate by Gentile Fusillo et al. (2021). The details of these 35 sources, along with their references, are also given in Table A1.

3.2. Disentangling main-sequence and white dwarf sources

As seen with the literature cross-match, we expected to find MS, RGB, and WD sources in our sample. With the exceptional astrometry from *Gaia*, we created a *Gaia* colour-magnitude diagram (CMD) and segregated the sample of MS and WD sources based on their positions in the CMD.

We plot the absolute *G*-band magnitude M_G against $G_{BP} - G_{RP}$ colour for 273 sources in Fig. 3 along with the zero-age main sequence (ZAMS) (Pecaut & Mamajek 2013), a 100 Myr isochrone from the code modules for experiments in stellar astrophysics (MESA)[2] (Choi et al. 2016; Dotter 2016), and WD cooling tracks from Bédard et al. (2020). The CMD shows a diverse population including WDs, MS stars, and potential WD+MS star systems. A clear distinction is visible in the CMD, and we used $G_{BP} - G_{RP} > 0.4$ mag as the cutoff to separate MS and WD sources (shown as regions A and B, respectively). The bottom panel in Fig. 3 shows a clear distinction between the population at $G_{BP} - G_{RP} = 0.4$. This distinction aligns with the expected optical brightness contrast between MS stars and WDs, enabling a reliable differentiation. This approach is based on the fact that WDs are brighter in bluer bands and MS stars are brighter in redder bands. WDs emit a significant amount of their radiation in the blue and ultraviolet parts of the spectrum. As a result, they tend to be brighter in the bluer bands (in this case, BP mag) than MS stars. The cutoff yielded 95 potential WD sources in region B and 178 potential MS stars in region A that exhibit characteristics consistent with MS stars. The SMC is characterised by a notably low foreground extinction value of $E(B - V) = 0.02$ mag (Hutchings 1982), representing the maximum potential extinction that our sources can encounter in this line of sight. Hence, for the purposes of our analysis, we considered an extinction value of $A_V = 0.062$ mag, which corresponds to $E(B - V) = 0.02$ mag for the sources.

3.3. Spectral energy distribution analysis of UV-bright main-sequence and white dwarf sources

To characterise the 178 potential MS sources, we employed a Python-based routine tailored to fit observed SEDs, similar to the SED routine used in Arun et al. (2021), Bhattacharyya et al. (2022), and Shridharan et al. (2022). The SED for a target object was constructed using photometric data from various
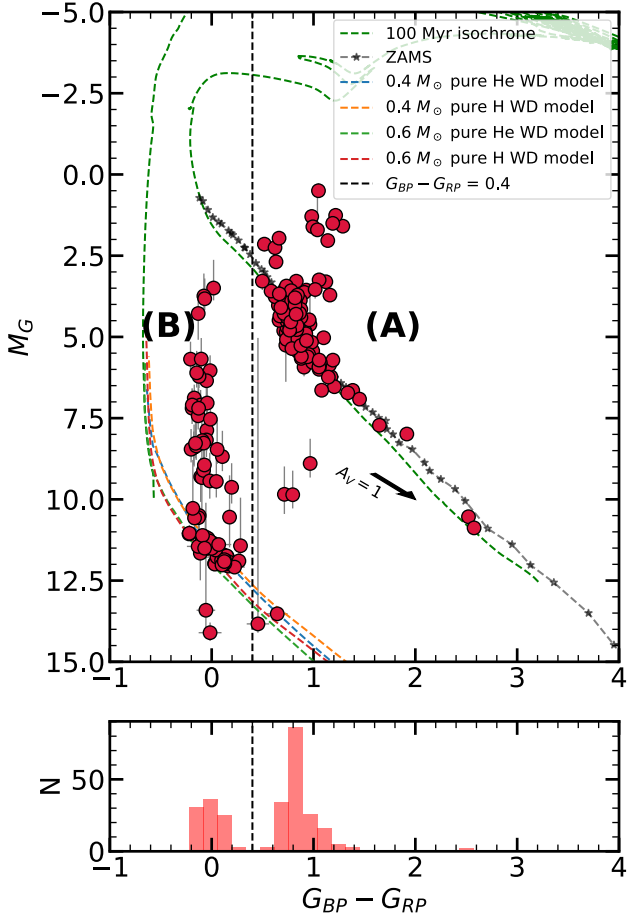
---

[2] https://waps.cfa.harvard.edu/MIST/

Fig. 3. Extinction-corrected *Gaia* CMD of the 273 sources (filled red circles) with $G_{BP} - G_{RP}$ on the *x*-axis and M_G on the *y*-axis is shown in the top panel. The vertical black line that divides the CMD into two populations, is at $G_{BP} - G_{RP} = 0.4$. The black arrow shows the reddening vector for $A_V = 1$ mag. The Number distribution of the 273 sources in the $G_{BP} - G_{RP}$ colour is shown in the bottom panel

sources spanning wavelengths from the far-UV to far-IR, including available photometry from UVIT, The fourth U.S. Naval Observatory CCD Astrograph Catalog (UCAC4), SDSS, *Gaia*, the Two Micron All Sky Survey (2MASS), AKARI Infrared Camera (IRC), AKARI Far-Infrared Surveyor (FIS), the Wide-Field Infrared Survey Explorer (WISE), and The Infrared Astronomical Satellite (IRAS). The SED templates used for the fitting process were derived from the BT-NextGen (AGSS2009) model grid (Allard et al. 2011, 2012), considering an effective temperature ($800 K \leq T_{eff} \leq 70000$ K), a surface gravity ($-0.5 \leq \log g \leq 6$), and a metallicity ($-4 \leq$ [Fe/H] ≤ 0.5).

The fitting procedure involved a normalisation process of observed and model photometry, using user-specified bands. The determination of the best-fit model relied on minimising the chi-squared parameter (χ^2), computed from fitting the UVIT bands, *Gaia* G-, G_{BP}-, and G_{RP}-band photometry, thereby giving the most suitable model corresponding to the lowest χ^2. Subsequently, stellar parameters such as T_{eff} and $\log g$ were estimated from the SED fitting. Upon visual inspection of the fit quality, our analysis revealed that 161 sources out of 178 exhibited a very good fit with theoretical models, which is indicative of their classification as UV-bright MS stars (provided in Table B1). About 89% of the 161 sources have $\log g$ ranging from 4 to 5.5. The T_{eff} of these sources ranges from 4500 K to 6500 K. Conversely,

16 stars encountered fitting discrepancies that can primarily be attributed to problematic photometric data or to a companion. They are further analysed in Sect. 3.4.

To characterise the WD sources, we fitted the Koester WD models for pure H atmospheres (Koester 2010) to the 95 sources lying in region B of the *Gaia* CMD. The fitting process involved a systematic comparison between observed SEDs and theoretical WD models. By assessing various parameters, such as T_{eff} and $\log g$, the routine determines the most suitable WD model that matches the observed data best. Subsequently, the fitted SEDs underwent a visual classification, and we categorised them based on the goodness of their fit. Forty-three of 95 sources showed a very good SED fit, indicating that they are highly probable WD candidates. By checking against the literature, we found that 37 out of these 43 WDs are new detections. Four sources (*Gaia* DR3 4690615216552295808, *Gaia* DR3 4690615560150914560, *Gaia* DR3 4690613017528995840, and *Gaia* DR3 4690659300093357184) were previously classified as highly probable WD candidates by Gentile Fusillo et al. (2021), and two sources (*Gaia* DR3 4690616659661394304, *Gaia* DR3 4690551758417486336) were classified as WD candidates by Jackim et al. (2024). These are marked in boldface in Table 1. Furthermore, the stellar parameters encompassing critical factors such as effective temperature and surface gravity for the identified 43 WDs are tabulated in Table 1. The SED analysis resulted in 52 sources that we were unable to fit with a single WD model. Some of these sources showed optical or IR excess. These objects are studied in detail in the next section as potential WD+MS sources.

3.4. Identifying white dwarf+main sequence binaries

The WD+MS binaries pose a unique challenge since the flux of one of the stars dominates the SED, making their identification in the HR diagram elusive. The magnitudes and colours of these systems are similar to those of single stars. However, systems where the WD and MS companion both contribute significantly to the optical flux form a bridge between the WD and MS loci in the CMD (Rebassa-Mansergas et al. 2021). Our initial analysis revealed that our sample may also include WD+MS binary systems since some objects lie between the WD locus denoted by the WD cooling tracks and the MS loci indicated by the ZAMS in Fig. 3 displaying the CMD.

Our strategy involved visually classifying SEDs showing optical and IR excess during the WD model fitting or the sources that did not fit the single WD model well as potential binary systems. This resulted in the identification of 52 such sources. Using the VO SED analysing tool (VOSA[3]; Bayo et al. 2008), we fitted binary models for these candidates. For the MS star component in our binary modelling, we used the BT-Settl-CIFIST models (Baraffe et al. 2015), which offer a wide database of spectra across T_{eff} ranging from 1200 K to 7000 K, with $\log g$ within $4 \leq \log g \leq 5$. For H-rich WDs, we employed Koester (2010) WD evolution models (Koester 2010), with T_{eff} between 5000 K and 80 000 K and $\log g$ within $6.5 \leq \log g \leq 9.5$.

Visual inspection revealed that 13 of the 52 stars had a good fit, which means that they are potential binary systems. A representative sample of a well-fitted WD+MS system is shown in the bottom panel of Fig. 4. Table 2 presents the parameters of these selected WD+MS binary candidates. Notably, we refrained from relying on reduced χ^2 parameter provided by VOSA. Existing literature (Rebassa-Mansergas et al. 2021; Nayak et al. 2024)

---

[3] http://svo2.cab.inta-csic.es/theory/vosa/

Table 1. First ten rows from the list of 43 single WDs.

RA (deg)	DE (deg)	Distance (pc)	N263M (mag) AB	N263M (mag) Error	N245M (mag) AB	N245M (mag) Error	N279N (mag) AB	N279N (mag) Error	F172M (mag) AB	F172M (mag) Error	F169M (mag) AB	F169M (mag) Error	F154W (mag) AB	F154W (mag) Error	N219M (mag) AB	N219M (mag) Error	Teff (K)	log g	Cooling Age (Gyr)	WD Mass ($M_\odot$)
17.80608 [β]	**−71.47253**	1173^{+336}_{-219}	**18.959**	**0.035**	**18.944**	**0.03**	**19.067**	**0.069**	**19.078**	**0.057**	**19**	**0.046**	**19.099**	**0.045**	**18.957**	**0.064**	**13250**	**8.25**		**ELM**
16.71119 [α]	**−71.31982**	1554^{+436}_{-278}	**18.639**	**0.03**	**18.767**	**0.028**	**18.618**	**0.055**	**18.784**	**0.049**	**18.867**	**0.039**	**19.071**	**0.044**	**18.782**	**0.053**	**12000**	**7.25**		**ELM**
17.15645 [α]	**−71.33187**	1860^{+526}_{-416}	**18.827**	**0.019**	**18.855**	**0.017**	**18.877**	**0.036**	**18.869**	**0.03**	**18.884**	**0.024**	**18.931**	**0.024**	**18.773**	**0.032**	**14250**	**9**		**ELM**
17.15341	−71.33289	557^{+66}_{-20}	20.5	0.042	20.709	0.04	20.435	0.078	20.732	0.074	20.822	0.06	20.957	0.063	20.335	0.066	12500	8.5	0.14	0.59
17.31568 [α]	**−71.35908**	1889^{+512}_{-298}	**18.928**	**0.02**	**19.056**	**0.019**	**19.084**	**0.04**	**19.128**	**0.034**	**19.228**	**0.028**	**19.274**	**0.028**	**18.976**	**0.035**	**12500**	**8**		**ELM**
17.24697 [β]	**−71.31595**	1119^{+420}_{-238}	**18.691**	**0.018**	**18.8**	**0.016**	**18.748**	**0.034**	**18.814**	**0.029**	**18.888**	**0.024**	**18.918**	**0.024**	**18.763**	**0.032**	**13500**	**8.5**		**ELM**
17.13819	−71.2866	524^{+68}_{-25}	20.821	0.05	20.806	0.042	20.857	0.112	20.911	0.076	21.068	0.078	21.227	0.072	20.666	0.128	11500	7.25	0.31	0.57
17.9879 [α]	**−71.32667**	1729^{+829}_{-335}	**19.066**	**0.026**	**19.249**	**0.025**	**19.092**	**0.051**									**11500**	**8.5**		**ELM**
17.54867	−71.16241	422^{+35}_{-23}	21.12	0.068	21.095	0.058	20.9	0.115	21.382	0.162	21.328	0.124	21.599	0.142			10750	6.5	0.52	0.44
17.40706 [γ]	−71.45349	269^{+16}_{-26}	18.76	0.019	18.91	0.017	18.757	0.034	19.112	0.033	19.132	0.027	19.245	0.028	18.887	0.043	11500	7.25	0.24	0.49

Notes. The whole table is available at the CDS. The WDs marked in bold were previously detected in the literature as WD candidates. [α]Gentile Fusillo et al. (2021), [β]Jackim et al. (2024), [γ]WD showing IR excess.
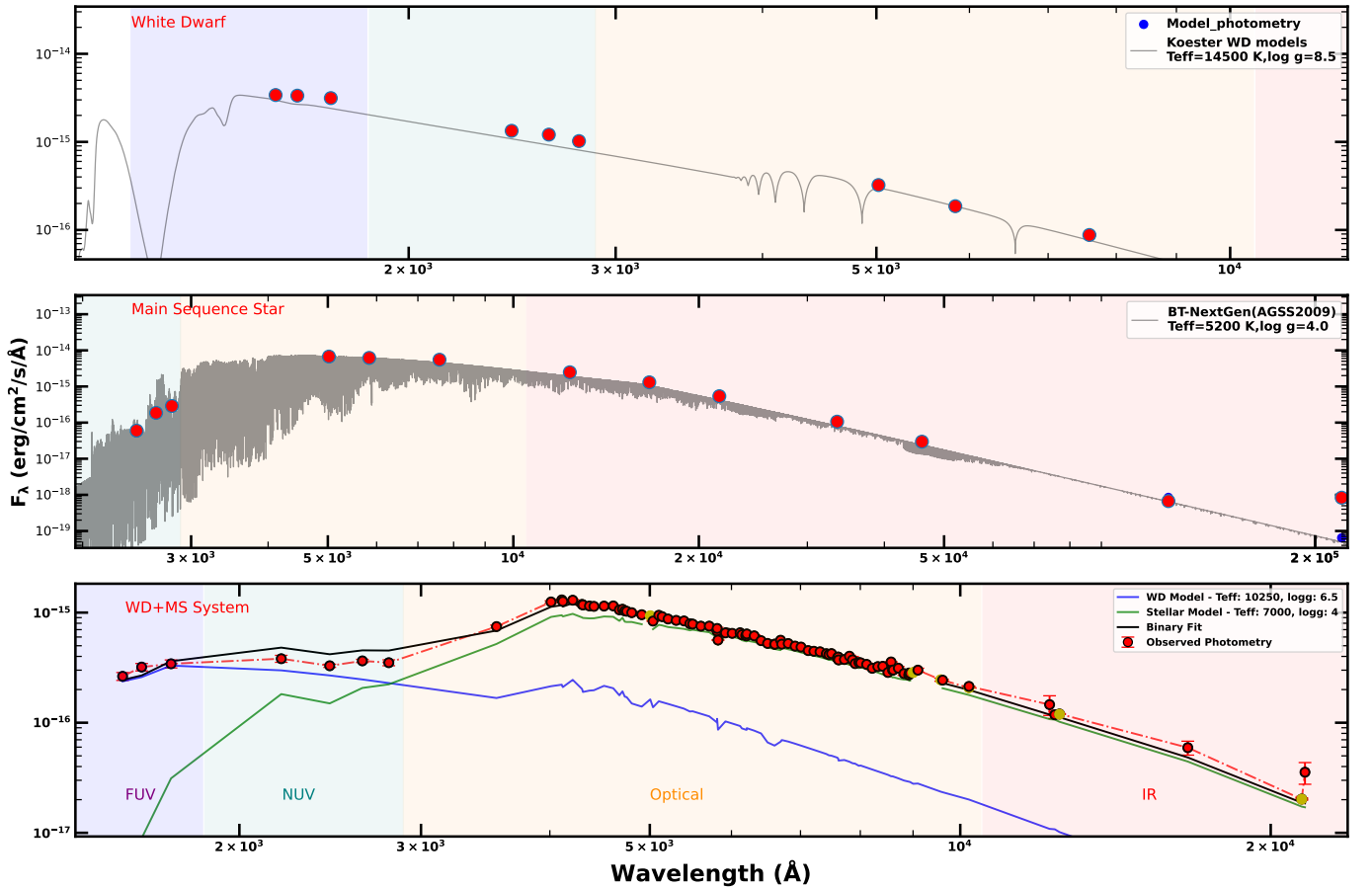

Fig. 4. Representative sample of the SEDs of WDs (*Gaia* DR3 4690625700572457088), MS stars (*Gaia* DR3 4690614052626726016), and WD+MSs (*Gaia* DR3 4690657483318685312) over-plotted with their respective best-fit models. The scaling of the *x*-axis and *y*-axis of each plot is different.

Table 2. List of the 13 WD+MS candidates identified with the parameters of the MS and WD components.

| RA (deg)	DE (deg)	Distance (pc)	N263M (mag) AB	N263M (mag) Error	N245M (mag) AB	N245M (mag) Error	N279N (mag) AB	N279N (mag) Error	F172M (mag) AB	F172M (mag) Error	F169M (mag) AB	F169M (mag) Error	F154W (mag) AB	F154W (mag) Error	N219M (mag) AB	N219M (mag) Error	MS_Teff (K)	MS_logg	WD_Teff (K)	WD_logg	WD Cooling Age (Gyr)	WD Mass ($M_\odot$)
17.58841	−71.29290	430^{+27}_{-28}	21.227	0.059	21.372	0.054			21.581	0.129	21.919	0.117	21.904	0.117	20.976	0.105	7000	4.5	13750	9.5	0.50	0.46
17.27154	−71.51881	413^{+21}_{-20}	21.18	0.098	21.216	0.087			21.521	0.175	21.269	0.13	21.293	0.123			6800	4	12250	6.5	0.50	0.47
17.00401	−71.48322	428^{+26}_{-30}	21.41	0.107	21.472	0.097			21.689	0.143	21.98	0.169					7000	4	11000	6.5	0.44	0.43
17.29824	−71.40148	464^{+19}_{-12}	21.782	0.129	21.789	0.112	21.485	0.204	21.988	0.145	21.95	0.162	21.949	0.119			5800	4	11250	6.5	0.52	0.49
17.67229	−71.33692	397^{+18}_{-29}	21.394	0.081	21.664	0.076	21.109	0.134	21.433	0.166	21.823	0.156					6700	4	11750	6.5	0.50	0.43
17.33770	−71.38375	1022^{+349}_{-235}			21.482	0.097			22.074	0.173							7000	4	10250	6.5		ELM
16.96834	−71.38353	452^{+26}_{-33}	21.476	0.112	21.456	0.058	21.129	0.173	21.956	0.139	22.014	0.17	22.131	0.137			7000	4.5	12000	7.75	0.55	0.49
17.51080	−71.21059	429^{+18}_{-12}			21.961	0.121					22.926	0.22					7000	4	10500	6.5	0.59	0.42
17.38071	−71.19201	327^{+46}_{-31}	21.135	0.071	21.32	0.069	21.213	0.133	21.822	0.149	22.325	0.196	22.123	0.135	21.043	0.15	7000	4.5	13250	9.5	0.49	0.32
17.95762	−71.46028	429^{+26}_{-26}	21.352	0.106	21.298	0.09			21.579	0.18	21.779	0.165					7000	4	14500	9.5	0.57	0.55
17.79306	−71.38791	464^{+10}_{-42}	21.603	0.119	21.507	0.099			21.925	0.208							7000	4	11000	6.5	0.47	0.47
17.71227	−71.29982	422^{+41}_{-22}	21.118	0.057	21.295	0.054	21.195	0.178	21.333	0.161	21.385	0.094	21.473	0.095			6900	5	12500	7.75	0.55	0.58
17.77915	−71.26768	431^{+33}_{-14}			21.762	0.111					22.699	0.233					7000	5	10500	6.5	0.55	0.52
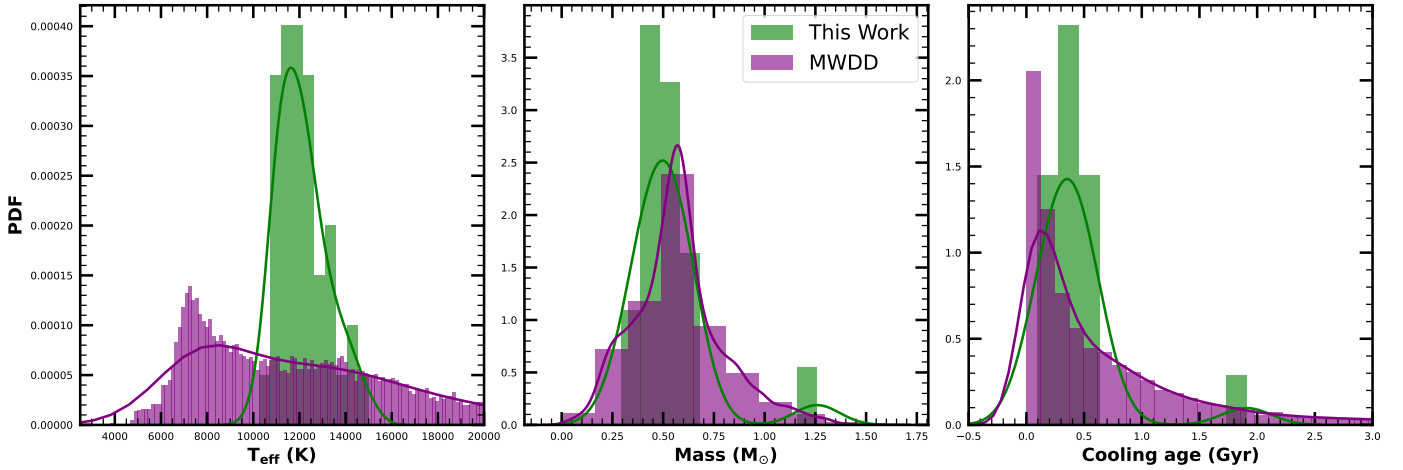
Fig. 5. Comparison of T_{eff} (K), mass ($M_\odot$) and the cooling age (Gyr) for single WDs identified in this work (green) and MWDD (purple). The kernel density estimates of the distributions are also overlaid for better visual representation.

has cautioned against their use due to potentially misleading outcomes. Instead, we used the prevalent and accepted parameter called visual goodness-of-fit (Vgf_b) provided by VOSA and visually inspected the goodness of fit in our analysis. All 13 candidates have $Vgf_b < 15$, which is usually considered as a proxy for well-fitted SEDs.

3.5. Estimation of mass and the cooling age of white dwarf and white dwarf+main sequence candidates

The determination of WD masses is crucial for understanding their physical properties and evolution. While the mass can be derived during SED fitting, its accuracy heavily depends on the derived $\log g$ of the WD. However, since the SED is essentially a low-resolution spectrum, the $\log g$ derived from SED fitting may not be precise, which leads to unreliable mass estimates.

To overcome this limitation, we adopted a method that is commonly used in the literature (e.g. Nayak et al. 2024; Karinkuzhi et al. 2024) that uses the model cooling curves of WDs to estimate their masses. For this purpose, we used the WD_models Python open-source package[4], which facilitates the conversion between WD optical photometry and physical parameters (Cheng et al. 2020). Specifically, we employed the cooling models developed by Bédard et al. (2020)[5], which account for WDs with thick H atmospheres and CO cores. WD_models estimates the mass and other parameters by finding the closest atmosphere grid and cooling model in the *Gaia* CMD.

By applying this method, we estimated the masses of 43 single WDs using their *Gaia* photometry. Nineteen of these WDs lie within the mass range covered by the available models, which spans from 0.2 $M_\odot$ to 1.3 $M_\odot$. Consequently, we estimated the masses for these 18 WDs. However, the masses of the remaining 24 WDs are below 0.2 $M_\odot$ and their luminosities exceed the model evolutionary tracks. As a result, we cannot estimate the masses for these sources through this method. Furthermore, we estimated the mass of the WD component of the 13 WD+MS candidates identified in this paper using the same method. We find that 12 of 13 sources lie within the model range, and we estimated the masses for them. One WD+MS candidate has a mass below 0.2 $M_\odot$ and its mass cannot be calculated for the same

reason mentioned earlier. The WD component masses range between 0.3 $M_\odot$ to 0.6 $M_\odot$.

In addition to the WD masses, we also estimated the cooling age of these WDs from the model tracks using the WD_models package. The cooling age of the single WDs ranges from 0.1 Gyr to 1.9 Gyr, and for the WD components of the WD+MS binaries, the cooling ages range from 0.2 Gyr to 0.6 Gyr. The mass and cooling age of single WDs and the WD+MS components are given in Tables 1 and 2, respectively.

3.6. Comparison with existing white dwarf and white dwarf+main sequence catalogues

It is important to compare the derived values of our sample to the values present in the literature on WDs. We made use of the Montreal White Dwarf Database[6] (Dufour et al. 2017), a collection of confirmed WDs in the literature. We selected single DA WDs with at least one spectra available as our bona fide sample of WDs. We also removed WDs with an IR excess or a debris disk. This criterion was met by 18448 WDs (hereafter, MWDD).

Figure 5 shows the comparison of T_{eff}, mass, and the cooling age (Gyr) for single WDs in this study (green) with those found in the MWDD (purple). It is evident from the distributions that we identify hotter and slightly lower-mass WDs than MWDD. Considering that the majority of MWDD WDs are identified using optical surveys such as SDSS, we enhanced the sensitivity using UVIT to the hotter WDs. We found the cooling ages of our WDs to be similar to the WDs identified in the literature.

Furthermore, we compared the WD components of our WD+MS candidates with the most recent WD+MS catalogue provided by Nayak et al. (2024) and Rebassa-Mansergas et al. (2021). Both these studies reported WD+MS candidates within 100 pc. While Rebassa-Mansergas et al. (2021) used the *Gaia* DR3 data for the identification of 112 WD+MS candidates, Nayak et al. (2024) used UV data from GALEX GR6/7 combined with *Gaia* DR3 to identify WD+MS candidates. Rebassa-Mansergas et al. (2021) targeted sources detected in *Gaia* optical CMD between the MS and the WD cooling sequence. Their 112 WD+MS candidates all belong to the region between MS and WDs on *Gaia* CMD, making them more sensitive to sources in which the WD and the MS share similar
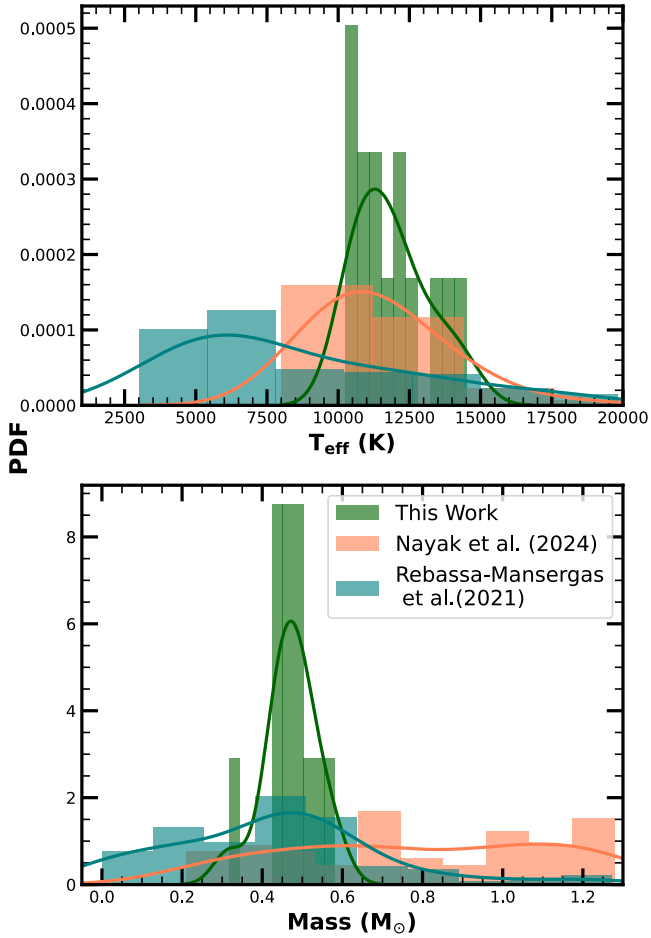
---

[4] https://github.com/SihaoCheng/WD_models

[5] Available at http://www.astro.umontreal.ca/~bergeron/CoolingModels/

[6] https://www.montrealwhitedwarfdatabase.org/home.html

Fig. 6. Comparison of T_{eff} (K) and mass ($M_\odot$) of the WD component of the WD+MS candidates identified in this work with the works of Rebassa-Mansergas et al. (2021) and Nayak et al. (2024).

contributions to the overall optical flux. On the other hand, Nayak et al. (2024) reported WD+MS candidates in the WD locus in UV CMD and the MS locus in the optical CMD. Our WD+MS binaries fall in the WD region of the *Gaia* CMD. Hence, the WD+MS population identified in this work is complementary to the sample detected by Rebassa-Mansergas et al. (2021) and Nayak et al. (2024). Figure 6 shows the comparison between the T_{eff} and mass of WDs in WD+MS systems identified in all three works. We find WDs with masses comparable to those of Rebassa-Mansergas et al. (2021), but less massive than the WDs found by Nayak et al. (2024). We identified hotter WDs than either of the previous studies.

4. Discussion

In this section, we discuss the population of WDs that do not fall in the WD locus and present the potential identification of a sample of ELMs in our sample. Furthermore, with the identified sample of WDs, we calculate the WD space density and compare it with previous estimates.

4.1. Extremely low-mass white dwarf candidates

The ELMs represent an exotic subset of WDs with masses below 0.3 $M_\odot$. These masses challenge the conventional understanding

of single stellar evolution. These objects are expected to form via binary mass transfer from the WD progenitor during its red giant branch phase either through Roche-lobe overflow or common-envelope evolution (Istrate et al. 2014a,b; Nandez et al. 2015; Li et al. 2019; Pelisoli & Vos 2019; Brown et al. 2022; Nayak et al. 2024; Khurana et al. 2023; Chen et al. 2021, 2022). Kilic et al. (2007) established a minimum mass threshold of ~0.3 $M_\odot$ for WDs that formed through standard evolutionary channels, considering the age of the Universe and associated timescales. Objects falling below this threshold necessitate alternative formation mechanisms, often linked to binary or multiple stellar systems. The mass and radius of a WD are inversely related (Parsons et al. 2017; Bédard et al. 2017). This implies that the ELMs exhibit larger radii, making them brighter than their canonical counterparts. Consequently, they occupy an intermediate region in the CMD, positioned between the MS locus and the locus of single WDs.

Pelisoli & Vos (2019) defined a specific region in the *Gaia* CMD to identify the locus where ELMs are expected to appear. This region is defined by the equations

$$M_G < 5.25 + 6.94 \, (G_{BP} - G_{RP} + 0.61)^{1/2.32} \quad (1)$$

$$M_G > 1.15 \, (G_{BP} - G_{RP}) + 6.00 \quad (2)$$

$$M_G > -42.2 \, (G_{BP} - G_{RP})^2 + 83.8(G_{BP} - G_{RP}) - 20.1, \quad (3)$$

where M_G is the absolute G magnitude calculated using the *Gaia* G-band magnitude.

As mentioned in Sect. 3.5, the masses of 25 WDs (24 single WDs and one WD+MS candidate) could not be found due to their higher luminosity. In Fig. 7, we plot the above-defined ELM region on the *Gaia* CMD. Twenty of these 25 high-luminosity WDs fall within the defined ELM region. These 20 WDs are strong candidates for ELMs and are marked by ELM in the WD Mass column of Tables 1 and 2. They need to be followed up by spectroscopic observations to verify their candidacy. Follow-up studies of these 20 candidates will also allow us to constrain their physical parameters. The median distance of the canonical-mass WD sources in this study is ~500 pc, and for the ELM candidates, the median distance is ~1500 pc. We observe a higher percentage of ELMs in this study because ELMs are brighter than canonical-mass WDs, resulting in better *Gaia* quality compared to WDs at a similar distance. Except for the extreme mass loss observed in high-metallicity stars (Kilic et al. 2007), ELM WDs are thought to originate from binary evolution, involving one or more instances of common-envelope evolution (Li et al. 2019). Therefore, investigating ELM systems can provide valuable insights into the wider realm of binary interactions.

4.2. Completeness of the white dwarf detection

Ultraviolet missions such as GALEX and the UV-Excess survey (UVEX; Groot et al. 2009) have been instrumental in studying the hot DA WD population within 1kpc of the Sun. Based on the photometrically identified DA population with $T_{eff} > 10\,000$ K, the estimate of the WD stellar density is ~2.9–3.8 × 10^{-4} pc^{-3} within 1kpc (Verbeek et al. 2013). Hence, considering a cone with a radius of 40′ (FoV) at a distance of 1kpc, we can expect 48 DA WDs hotter than 10 000 K. Using UVIT, we find 22 WDs hotter than 10 000 K within 1kpc, providing a crude completeness estimate of 46% percentage.
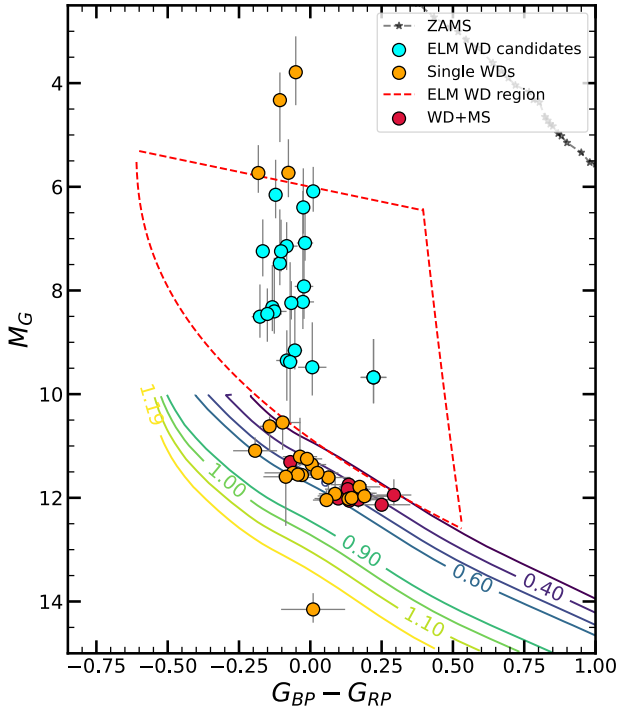
Fig. 7. Extinction-corrected *Gaia* CMD of single WDs and WD+MS candidates from our classification. The ELM region is marked with dotted red lines. ELM WD candidates are shown with filled cyan circles. The remaining single WDs and WD+MS candidates are shown with filled orange and red circles, respectively. The WD cooling models for different masses from Bédard et al. (2020) are also overlaid. The numbers on the cooling track denote their corresponding masses in $M_\odot$.

However, it should also be noted that we only considered stars with good-quality *Gaia* astrometry and photometry. As shown in Fig. 2, a large population of sources lies at distances smaller than 2kpc that did not satisfy our quality criteria. This population might have many new WDs with low-quality *Gaia* astrometry and photometry. Upon relaxing the ϖ/σ_ϖ cutoff from ≥ 3 to ≥ 1, we additionally find 552 WD candidates with an exceptional fit to the WD models in the SED analysis. The distance estimates provided by *Gaia* DR3 would not be accurate for these distant low-luminosity sources. Based on the SED fit, these 552 sources have T_{eff} in the range of 7250 K to 30 000 K. Considering the UVIT sensitivity and degeneracies in mass, radius, and log$g$, we estimate that they can only be detected to a distance limit of 8–10 kpc based on the flux values of the Koester (2010) model of a 30 000 K WD. Assuming 8 kpc as the maximum distance of 552 WD candidates, we can estimate an upper limit to the WD stellar density of ~ 5–6×10^{-4} pc^{-3}. Taking an alternative approach, when we consider the distances provided by *Gaia* DR3 for the low-quality WDs, then 181 WDs are present within 1kpc. Under the assumption that the WDs density is homogeneous and isotropic throughout 1kpc, the space density reaches $\sim 1.3 \times 10^{-3}$ pc^{-3}, which is higher than most of the literature estimates given in Verbeek et al. (2013, Table 3). Our upper limit of global (up to 1 kpc) WD space density agrees with the local (<20pc) WD space density ($\sim 4 \times 10^{-3}$ pc^{-3}) estimated using *Gaia* EDR3 by Gentile Fusillo et al. (2021). This shows the need for deep UV photometry to identify Galactic WDs. However, it is well known throughout the literature that the WD population model changes with the thin disc, thick disc, and the halo (Bianchi et al. 2011). Hence, it is clear that UV photometry, in combination with *Gaia* future releases, can be used to estimate the space density of WDs better, given the structure of the

Galaxy. Large-scale WD detection studies combining UV and *Gaia* are necessary to accurately estimate the WD density in the Galaxy. Future *Gaia* data releases will constrain the astrometry of these low-quality WDs better.

5. Summary

We have demonstrated the capabilities of UVIT to identify and characterise the WDs in the Galaxy. We made use of the UVIT point-source catalogue published by Devaraj et al. (2023) observed towards the outskirts of the SMC region. Furthermore, we cross-matched the UVIT photometry with *Gaia* DR3 and found that the 273 UV sources with good-quality *Gaia* astrometry and photometry values belong to the Milky Way galaxy rather than to the SMC region. Using colour cuts and an SED analysis, we identified 43 single WDs (given in Table 1) in a region in which only 6 WDs were previously detected as WD candidates based on the *Gaia* DR3 analysis (Gentile Fusillo et al. 2021; Jackim et al. 2024). In addition to the 43 WDs, we reported the identification of 13 WD+MS candidates (Table 2) and 161 UV-bright MS stars (Table B.1).

To estimate the physical characteristics of the identified WDs in our sample, we followed a method that is commonly adopted in the literature (Nayak et al. 2024; Karinkuzhi et al. 2024) using the `WD_models` open-source Python package. The package estimates the mass and age of the WDs by finding the closest atmosphere grid and cooling model based on the position in the *Gaia* CMD. We find that the masses of WDs identified in this study range from 0.2 $M_\odot$ to 1.3 $M_\odot$ and the T_{eff} from 10 000 K to 15 000 K. The cooling ages of these WDs range from 0.1 Gyr to 2 Gyr. In comparison to the bona fide sample of WDs (MWDD), we find that our sample of WDs has higher temperatures owing to the detection through UVIT. We note that the estimated mass and the cooling age of WDs identified in this work match the literature values from MWDD well. Furthermore, we reported the detection of 20 ELM candidates based on their position in the *Gaia* CMD and SED analysis. Further detailed studies and spectroscopic confirmation of these sources will lead to a better understanding of their formation processes. Given the limitations of *Gaia* DR3 distance measurements of optically faint WDs, we discussed the completeness and estimates of the WD space density through our sample. Approximate calculations showed that the estimated WD space density within 1 kpc can be two orders of magnitude larger than previous estimates.

Our results not only highlight the instrumental effectiveness of the UVIT, but also anticipate the potential of upcoming dedicated UV missions such as the INSIST. These missions are premier instruments for the systematic discovery of WDs and other diverse stellar systems, providing invaluable insights into the complex dynamics of binary systems within our galaxy. As we conclude this study within the current FoV, our analytical approach will be extended to unveil additional WD systems in other fields observed by UVIT (Piridi et al. 2024; Mondal et al. 2023; Leahy et al. 2020). The subsequent phase involves the critical follow-up step of spectroscopic surveys. This effective blend of follow-up observations and thorough analysis establishes the UVIT and upcoming missions as crucial contributors to enhancing our understanding of stellar systems in the ultraviolet domain.

Data availability

Full Tables 1 and 2, as well as Tables A.1 and B.1, are available at the CDS via anonymous ftp to `cdsarc.cds.unistra.fr`

References

Allard, F., Homeier, D., & Freytag, B. 2011, in 16th Cambridge Workshop on Cool Stars, Stellar Systems, and the Sun, eds. C. Johns-Krull, M. K. Browning, & A. A. West, Astronomical Society of the Pacific Conference Series, 448, 91

Allard, F., Homeier, D., & Freytag, B. 2012, Philos. Transa. Roy. Soc. Lond. Ser. A, 370, 2765

Arun, R., Mathew, B., Maheswar, G., et al. 2021, MNRAS, 507, 267

Bailer-Jones, C., Rybizki, J., Fouesneau, M., Demleitner, M., & Andrae, R. 2021, AJ, 161, 147

Baraffe, I., Homeier, D., Allard, F., & Chabrier, G. 2015, A&A, 577, A42

Bayo, A., Rodrigo, C., y Navascués, D. B., et al. 2008, A&A, 492, 277

Bédard, A., Bergeron, P., & Fontaine, G. 2017, ApJ, 848, 11

Bédard, A., Bergeron, P., Brassard, P., & Fontaine, G. 2020, ApJ, 901, 93

Bhattacharyya, S., Mathew, B., Ezhikode, S. H., et al. 2022, ApJ, 933, L34

Bianchi, L. 2009, Astrophys. Space Sci., 320, 11

Bianchi, L., Efremova, B., Herald, J., et al. 2011, MNRAS, 411, 2770

Brown, A. G., Vallenari, A., Prusti, T., et al. 2021, A&A, 649, A1

Brown, W. R., Kilic, M., Kosakowski, A., & Gianninas, A. 2022, ApJ, 933, 94

Chen, H.-L., Tauris, T. M., Han, Z., & Chen, X. 2021, MNRAS, 503, 3540

Chen, H.-L., Tauris, T. M., Chen, X., & Han, Z. 2022, ApJ, 925, 89

Cheng, S., Cummings, J. D., Ménard, B., & Toonen, S. 2020, ApJ, 891, 160

Choi, J., Dotter, A., Conroy, C., et al. 2016, ApJ, 823, 102

Dattatrey, A. K., Yadav, R., Kumawat, G., et al. 2023a, MNRAS, 523, L58

Dattatrey, A. K., Yadav, R., Rani, S., et al. 2023b, ApJ, 943, 130

De Grijs, R., & Bono, G. 2015, AJ, 149, 179

Devaraj, A., Joseph, P., Stalin, C., Tandon, S. N., & Ghosh, S. K. 2023, ApJ, 946, 65

Dotter, A. 2016, ApJS, 222, 8

Dufour, P., Blouin, S., Coutu, S., et al. 2017, in 20th European White Dwarf Workshop, eds. P. E. Tremblay, B. Gaensicke, & T. Marsh, Astronomical Society of the Pacific Conference Series, 509, 3

Eisenstein, D. J., Liebert, J., Harris, H. C., et al. 2006, ApJS, 167, 40

Fontaine, G., Brassard, P., & Bergeron, P. 2001, PASP, 113, 409

Gaia Collaboration (Brown, A., et al.) 2018, A&A, 616

Gaia Collaboration (Vallenari, A., et al.) 2023, A&A, 674, A1

Gentile Fusillo, N. P., Tremblay, P.-E., Gänsicke, B. T., et al. 2019, MNRAS, 482, 4570

Gentile Fusillo, N., Tremblay, P.-E., Cukanovaite, E., et al. 2021, MNRAS, 508, 3877

Gómez de Castro, A. I., & Barstow, M. A. 2007, UV Astronomy: Stars from Birth to Death

Groot, P. J., Verbeek, K., Greimel, R., et al. 2009, MNRAS, 399, 323

Hutchings, J. 1982, ApJ, 255, 70

Istrate, A., Tauris, T., & Langer, N. 2014a, A&A, 571, A45

Istrate, A., Tauris, T., Langer, N., & Antoniadis, J. 2014b, A&A, 571, A3

Jackim, R., Heyl, J., & Richer, H. 2024, arXiv preprint [arXiv:2404.07388]

Jadhav, V. V., Sindhu, N., & Subramaniam, A. 2019, ApJ, 886, 13

Jiménez-Esteban, F., Torres, S., Rebassa-Mansergas, A., et al. 2018, MNRAS, 480, 4505

Karinkuzhi, D., Mukhopadhyay, B., Wickramasinghe, D., & Tout, C. A. 2024, MNRAS, 529, 4577

Kepler, S. O., Pelisoli, I., Koester, D., et al. 2016, MNRAS, 455, 3413

Kepler, S. O., Pelisoli, I., Koester, D., et al. 2019, MNRAS, 486, 2169

Kepler, S. O., Koester, D., Pelisoli, I., Romero, A. D., & Ourique, G. 2021, MNRAS, 507, 4646

Khurana, A., Chawla, C., & Chatterjee, S. 2023, ApJ, 949, 102

Kilic, M., Stanek, K., & Pinsonneault, M. 2007, ApJ, 671, 761

Koester, D. 2010, Mem. Soc. Astron. Ital., 81, 921

Kumar, A., Ghosh, S., Hutchings, J., et al. 2012, in Space Telescopes and Instrumentation 2012: Ultraviolet to Gamma Ray, 8443, SPIE, 455

Leahy, D. A., Postma, J., Chen, Y., & Buick, M. 2020, ApJS, 247, 47

Li, Z., Chen, X., Chen, H.-L., & Han, Z. 2019, ApJ, 871, 148

Mondal, C., Saha, K., Bhattacharya, S., et al. 2023, ApJS, 264, 40

Morrissey, P., Conrow, T., Barlow, T. A., et al. 2007, ApJS, 173, 682

Nandez, J. L., Ivanova, N., & Lombardi Jr, J. C. 2015, MNRAS, 450, L39

Nayak, P. K., Ganguly, A., & Chatterjee, S. 2024, MNRAS, 527, 6100

Panthi, A., & Vaidya, K. 2024, MNRAS, 527, 10335

Panthi, A., Subramaniam, A., Vaidya, K., et al. 2023, MNRAS, 525, 1311

Parsons, S., Rebassa-Mansergas, A., Schreiber, M. R., et al. 2016, MNRAS, 463, 2125

Parsons, S., Gänsicke, B. T., Marsh, T., et al. 2017, MNRAS, 470, 4473

Pecaut, M. J., & Mamajek, E. E. 2013, ApJS, 208, 9

Pelisoli, I., & Vos, J. 2019, MNRAS, 488, 2892

Piridi, S., Kumar, R., Pandey, D., & Pradhan, A. C. 2024, in 42nd meeting of the Astronomical Society of India (ASI, O46)

Prabhu, D. S., Subramaniam, A., Sahu, S., et al. 2022, ApJ, 939, L20

Rebassa-Mansergas, A., Ren, J., Irawati, P., et al. 2017, MNRAS, 472, 4193

Rebassa-Mansergas, A., Solano, E., Jiménez-Esteban, F. M., et al. 2021, MNRAS, 506, 5201

Ren, J.-J., Raddi, R., Rebassa-Mansergas, A., et al. 2020, ApJ, 905, 38

Sahu, S., Subramaniam, A., Singh, G., et al. 2022, MNRAS, 514, 1122

Shridharan, B., Mathew, B., Bhattacharyya, S., et al. 2022, A&A, 668, A156

Sindhu, N., Subramaniam, A., Jadhav, V. V., et al. 2019, ApJ, 882, 43

Stecher, T. P., Cornett, R. H., Greason, M. R., et al. 1997, PASP, 109, 584

Subramaniam, A., et al. 2018, MNRAS, 481, 226

Tandon, S., Hutchings, J., Ghosh, S., et al. 2017a, J. Astrophys. Astron., 38, 1

Tandon, S., Subramaniam, A., Girish, V., et al. 2017b, AJ, 154, 128

Tandon, S., Postma, J., Joseph, P., et al. 2020, AJ, 159, 158

Vaidya, K., Panthi, A., Agarwal, M., et al. 2022, MNRAS, 511, 2274

Verbeek, K., Groot, P. J., Nelemans, G., et al. 2013, MNRAS, 434, 2727

York, D. G., Adelman, J., Anderson Jr, J. E., et al. 2000, AJ, 120, 1579